

# Targeted elimination of tetravalent-Sn-induced defects for enhanced efficiency and stability in lead-free NIR-II perovskite LEDs

Received: 30 May 2024

Accepted: 4 November 2024

Published online: 15 November 2024



Xiang Guan<sup>1,2,4</sup>, Yuqing Li<sup>2,4</sup>, Yuanyuan Meng<sup>2</sup>, Kongxiang Wang<sup>1</sup>, Kebin Lin<sup>2</sup>, Yujie Luo<sup>1</sup>, Jing Wang<sup>1</sup>, Zhongtao Duan<sup>1</sup>, Hong Liu<sup>1</sup>, Liu Yang<sup>2</sup>, Lingfang Zheng<sup>2</sup>, Junpeng Lin<sup>2</sup>, Yalian Weng<sup>2</sup>, Fengxian Xie<sup>1</sup>✉, Jianxun Lu<sup>2,3</sup>✉ & Zhanhua Wei<sup>2</sup>✉

Eco-friendly Sn-based perovskites show significant potential for high-performance second near-infrared window light-emitting diodes (900 nm – 1700 nm). Nevertheless, achieving efficient and stable Sn-based perovskite second near-infrared window light-emitting diodes remains challenging due to the propensity of Sn<sup>2+</sup> to oxidize, resulting in detrimental Sn<sup>4+</sup>-induced defects and compromised device performance. Here, we present a targeted strategy to eliminate Sn<sup>4+</sup>-induced defects through moisture-triggered hydrolysis of tin tetrahalide, without degrading Sn<sup>2+</sup> in the CsSnI<sub>3</sub> film. During the moisture treatment, tin tetrahalide is selectively hydrolyzed to Sn(OH)<sub>4</sub>, which provides sustained protection. As a result, we successfully fabricate second near-infrared window light-emitting diodes emitting at 945 nm, achieving a performance breakthrough with an external quantum efficiency of 7.6% and an operational lifetime reaching 82.6 h.

In recent years, there has been considerable interest in near-infrared perovskite light-emitting diodes (NIR Pero-LEDs) due to their remarkable advancements in efficiency development.<sup>1–4</sup> Nevertheless, the emission of these high-efficiency devices is currently restricted to the first NIR window (NIR-I, 700–900 nm). In contrast, the second NIR window (NIR-II, 900–1700 nm) emission offers applications in night vision, biological tissue analysis, biometric recognition, and communication due to its advantages, such as invisible emission, deeper tissue penetration, and reduced scattering.<sup>5–9</sup> Despite these promising prospects, the fabrication of potential commercial NIR-II Pero-LEDs remains challenging because of the limitation of the emission spectrum and toxicity in Pb-based perovskite components.<sup>10</sup>

Recently, eco-friendly Sn-based Pero-LEDs emerged as a potential solution, featuring captivating NIR-II emission and showing significant progress in device efficiency.<sup>11–13</sup> However, despite achieving relatively

high device efficiency, organic-inorganic hybrid components have not satisfied the crucial criteria of emitting spectra (emitting peak > 900 nm) and operational lifetime.<sup>13,14</sup> In contrast, the all-inorganic Sn-based perovskite CsSnI<sub>3</sub> features enhanced stability, robust emission properties, and more favorable NIR-II emitting spectra compared to their organic-inorganic hybrid counterparts.<sup>12,15</sup> Therefore, the all-inorganic CsSnI<sub>3</sub>-based Pero-LEDs exhibited a preferable operational lifetime of 23.6 h and a decent device efficiency of 5.4% in our early work.<sup>16</sup> However, due to the pronounced non-radiative recombination loss and ionic migration caused by Sn<sup>4+</sup>-induced defects, the operational lifetime and maximum external quantum efficiency (EQE<sub>max</sub>) of NIR-II all-inorganic Sn-based Pero-LEDs are currently limited to 39.5 h<sup>17</sup> and 6.6%<sup>18</sup>, respectively. Previous reports have revealed the chemical instability of Sn<sup>2+</sup>, which is prone to losing its two active 5s electrons and getting oxidized to Sn<sup>4+</sup>.<sup>19</sup> This process results in heavy self-doping

<sup>1</sup>Institute for Electric Light Sources, Shanghai Engineering Research Center for Artificial Intelligence and Integrated Energy System, School of Information Science and Technology, Fudan University, Shanghai, China. <sup>2</sup>Xiamen Key Laboratory of Optoelectronic Materials and Advanced Manufacturing, Institute of Luminescent Materials and Information Displays, College of Materials Science and Engineering, Huaqiao University, Xiamen, China. <sup>3</sup>Division of Physical Science and Engineering, KAUST Catalysis Center (KCC), King Abdullah University of Science and Technology, Thuwal, Kingdom of Saudi Arabia. <sup>4</sup>These authors contributed equally: Xiang Guan, Yuqing Li. ✉e-mail: [xiefengxian@fudan.edu.cn](mailto:xiefengxian@fudan.edu.cn); [jianxun.lu@kaust.edu.sa](mailto:jianxun.lu@kaust.edu.sa); [weizhanhua@hqu.edu.cn](mailto:weizhanhua@hqu.edu.cn)

of  $\text{Sn}^{4+}$  and consequent substantial defects formation in Sn-based perovskites.<sup>20–23</sup> To address  $\text{Sn}^{4+}$ -induced defects, several precursor engineering strategies have been proposed to mitigate the oxidation from  $\text{Sn}^{2+}$  to  $\text{Sn}^{4+}$ , including solvent engineering,<sup>24–26</sup> additive engineering,<sup>14,27–30</sup> and component engineering.<sup>31,32</sup> In addressing solvent oxidation, Cho et al. selected Lewis base N,N'-dimethylpropyleneurea (DMPU) as a solvent, replacing the generally used dimethyl sulfoxide (DMSO). Since DMSO has been shown to induce solvent oxidation, resulting in the conversion of  $\text{Sn}^{2+}$  to  $\text{Sn}^{4+}$  during film annealing.<sup>21,33</sup> They demonstrated that Lewis base DMPU with strong coordination could suppress the  $\text{Sn}^{2+}$  oxidation in the precursor solution, yielding Pero-LEDs with an  $\text{EQE}_{\text{max}}$  of 0.361%. Moreover, Wei et al. analyzed the source of  $\text{Sn}^{4+}$  components, identifying thermal-induced disproportionation decomposition and surface oxidation as contributors to the formation of  $\text{Sn}^{4+}$  in perovskite films.<sup>22</sup> Consequently, they added a thermal sacrificial agent to the perovskite precursor solution to reduce disproportionation decomposition, achieving an improved EQE of 5.3% for the NIR-II Pero-LEDs. Although precursor engineering strategies have successfully mitigated  $\text{Sn}^{2+}$  oxidation, the presence of  $\text{Sn}^{4+}$  remains detectable in the active layer of the fabricated Pero-LEDs.<sup>14,22,33</sup> The reason is that, in these strategies,  $\text{Sn}^{2+}$  ions can still undergo oxidation after the formation of the active layer, losing the protection provided by the additives and solvents. The resulting  $\text{Sn}^{4+}$  continues to induce severe non-radiative recombination loss, leading to a decline in device performance. Urgently, a strategy needs to be developed to effectively eliminate  $\text{Sn}^{4+}$  defects in the Sn-based perovskite film and provide sustained protection.

In this study, we introduce an innovative targeted elimination strategy employing moisture-triggered tin tetrahalide ( $\text{SnX}_4$ ) hydrolysis to eliminate  $\text{Sn}^{4+}$  defects in the  $\text{CsSnI}_3$  film and provide sustained protection by forming  $\text{Sn}(\text{OH})_4$ . Specifically, during the moisture treatment process, the moisture selectively hydrolyzes the detrimental tin tetrahalide ( $\text{SnX}_4$ ) without degrading the  $\text{Sn}^{2+}$ , yielding hydrolysis product  $\text{Sn}(\text{OH})_4$ , which is promising to prevent the film from oxidants. So, the defects related to  $\text{Sn}^{4+}$  are significantly reduced, the non-radiative recombination is effectively inhibited, and the film quality is dramatically improved. As a result, employing the moisture treatment strategy significantly improves device efficiency and stability for the Pero-LEDs, with a NIR-II emission peak at 945 nm. These Pero-LEDs achieve a performance breakthrough with an  $\text{EQE}_{\text{max}}$  of 7.61% and a half-lifetime of 82.6 h. These results collectively indicate that the moisture-triggered hydrolysis of tin tetrahalide is a practical strategy for improving the performance and stability of Sn-based perovskite films and optoelectronic devices.

## Results and discussion

### Targeted elimination strategy for $\text{Sn}^{4+}$ defects

The heavy self-doping of  $\text{Sn}^{4+}$  in Sn-based Pero-LEDs can induce severe non-radiative recombination and aggravate device degradation.<sup>34</sup> However, as indicated by our previous study,<sup>22</sup> a considerable amount of  $\text{Sn}^{4+}$  remains in the perovskite film despite the introduction of reductants, antioxidants, and thermal-sacrificial agents into the  $\text{CsSnI}_3$  precursor solution to suppress  $\text{Sn}^{2+}$  oxidation (Fig. 1a). This is attributed to the fact that the  $\text{Sn}^{2+}$  in as-fabricated film is still prone to be oxidized after losing the protection of additives from precursor engineering, and these formed  $\text{Sn}^{4+}$  are inclined to accumulate on the film surface during the annealing process.<sup>22,31</sup> These aggregated  $\text{Sn}^{4+}$  on the surface continue to exert significant detrimental effects on the as-prepared  $\text{CsSnI}_3$  films.

In addressing this challenge, we introduced a targeted elimination strategy to eliminate  $\text{Sn}^{4+}$  defects in perovskite films by leveraging moisture to selectively induce hydrolysis of tin tetrahalide within the lattice, as illustrated in Fig. 1b. The schematic diagram of the moisture treatment process is presented in Supplementary Fig. 1. Following moisture treatment, detrimental  $\text{SnX}_4$  undergoes targeted elimination,

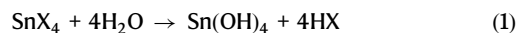
yielding  $\text{Sn}(\text{OH})_4$  and halogen hydride, effectively eliminating the  $\text{Sn}^{4+}$  defects without causing film degradation. Moreover, the formation of  $\text{Sn}(\text{OH})_4$  can provide sustained protection by blocking the oxidant erosion, leading to a marked increase in the  $\text{Sn}^{2+}$  proportion of  $\text{CsSnI}_3$  film. (Supplementary Fig. 2).

Notably, based on the optimal results, the  $\text{CsSnI}_3$  involving hydrolysis agents  $\text{SnCl}_2$  exhibited excellent performance after moisture treatment, thereby denoting  $\text{CsSnI}_3\text{-SnCl}_2$  in the following discussion.

### The effect of moisture treatment on the perovskite film

We performed X-ray photoelectron spectroscopy (XPS) to investigate the specific mechanism of hydrolysis reaction and its effects on the perovskite films. As illustrated in Fig. 2a, the pristine  $\text{CsSnI}_3\text{-SnCl}_2$  displays two distinct peaks at 486.4 eV and 487.4 eV, which are attributed to  $\text{Sn}^{2+}$  and  $\text{Sn}^{4+}$ , respectively. Additionally, a peak centered at 200.8 eV was identified and assigned to Cl 2p (Fig. 2b).

Following moisture treatment, the  $\text{Sn}^{4+}$  signal notably shifted toward a higher binding energy, from 487.4 eV to 487.6 eV, while the  $\text{Sn}^{2+}$  signal hardly moved. This indicates that moisture altered the chemical environment of  $\text{Sn}^{4+}$  but hardly affected  $\text{Sn}^{2+}$ , indicating that moisture selectively reacts with  $\text{Sn}^{4+}$ . The shift in the  $\text{Sn}^{4+}$  signal toward higher binding energy could be attributed to the formation of the hydrolysis product  $\text{Sn}(\text{OH})_4$ . Furthermore, the Cl signal disappeared after moisture treatment, indicating that the Cl<sup>−</sup> was hydrolyzed to HCl and thus evaporated, providing further evidence of the hydrolysis reaction (Fig. 2b). Notably, the emergence of the O 1s signal related to hydroxyl groups (−OH) after moisture treatment suggests the formation of  $\text{Sn}(\text{OH})_4$  during the hydrolysis reaction (Fig. 2c).<sup>35,36</sup> Additionally, the Cs 3d signal also hardly moved (Supplementary Fig. 3), while the I 3d signal showed a slight shift toward higher binding energy (Supplementary Fig. 4). These results support the conclusion that moisture treatment specifically targets  $\text{Sn}^{4+}$  and halide ions without degrading  $\text{Sn}^{2+}$  and  $\text{Cs}^+$ . Considering the characteristic ease of hydrolysis for  $\text{SnX}_4$ , the hydrolysis reaction can be described by the following Eq. (1):



To visually observe the hydrolysis reaction, the evolution of the  $\text{SnCl}_4$  hydrolysis process over time is depicted in Supplementary Fig. 5. The  $\text{SnCl}_4$  is a liquid at room temperature and readily undergoes hydrolysis upon exposure to moisture in the air. When pure water was introduced to a bottle containing  $\text{SnCl}_4$ , the solution exhibited a vigorous reaction, producing smoke-like HCl and water-insoluble  $\text{Sn}(\text{OH})_4$  on the bottle walls. This process is remarkably quick, completing in tens of seconds, highlighting the strong hydrolysis ability of  $\text{SnCl}_4$ , which rapidly forms hydroxide. In contrast, the hydrolysis rate of  $\text{SnI}_4$  is considerably slower. Upon adding pure water to a bottle containing  $\text{SnI}_4$  powder, the red  $\text{SnI}_4$  powder gradually transformed to transparent and insoluble  $\text{Sn}(\text{OH})_4$ , taking a time of 25 min. This indicates that  $\text{SnI}_4$  can undergo hydrolysis under  $\text{H}_2\text{O}$  induction, albeit at a much slower pace than  $\text{SnCl}_4$  (Supplementary Fig. 6). Based on these findings, we demonstrate that  $\text{SnX}_4$  can be hydrolyzed by water, and the degree of hydrolysis is influenced by the type of halide ion. Specifically, Cl<sup>−</sup> emerges as a potent hydrolysis reagent for  $\text{Sn}^{4+}$ , efficiently eliminating  $\text{Sn}^{4+}$  defects in  $\text{CsSnI}_3\text{-SnCl}_2$  films under moisture induction. The conclusion is also consistent with the results of Cl 2p core-level XPS spectra (Fig. 2b), in which the Cl<sup>−</sup> disappeared following moisture treatment.

To further verify the formation of  $\text{Sn}(\text{OH})_4$ , fourier transform infrared spectroscopy (FTIR) measurements were carried out. Our results clearly show the emergence of Sn-OH bending and stretching vibrations after moisture treatment, providing direct evidence of  $\text{Sn}(\text{OH})_4$  formation (Supplementary Fig. 7).<sup>37,38</sup> These combined

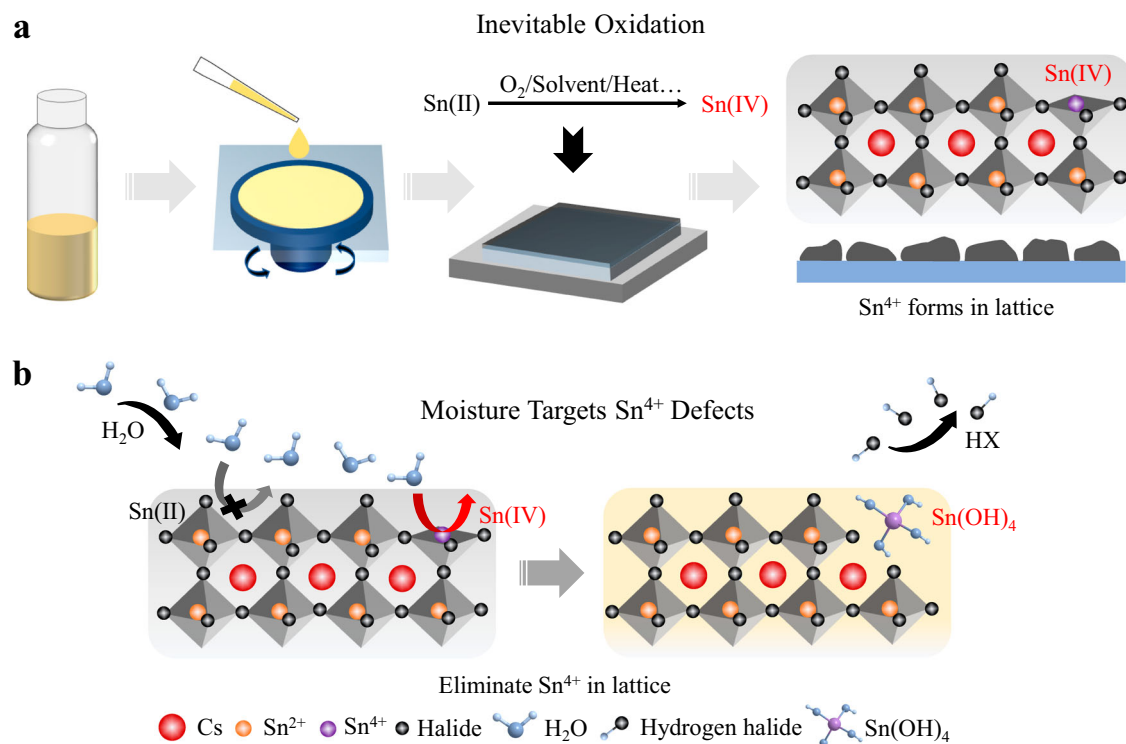


**Fig. 1 | Targeted elimination strategy for  $\text{Sn}^{4+}$  defects.** **a** Schematic diagram of the preparation of Sn-based perovskite film based on precursor engineering. **b** Schematic diagram of  $\text{SnX}_4$  hydrolysis induced by moisture post-treatment in  $\text{CsSnI}_3$  film.

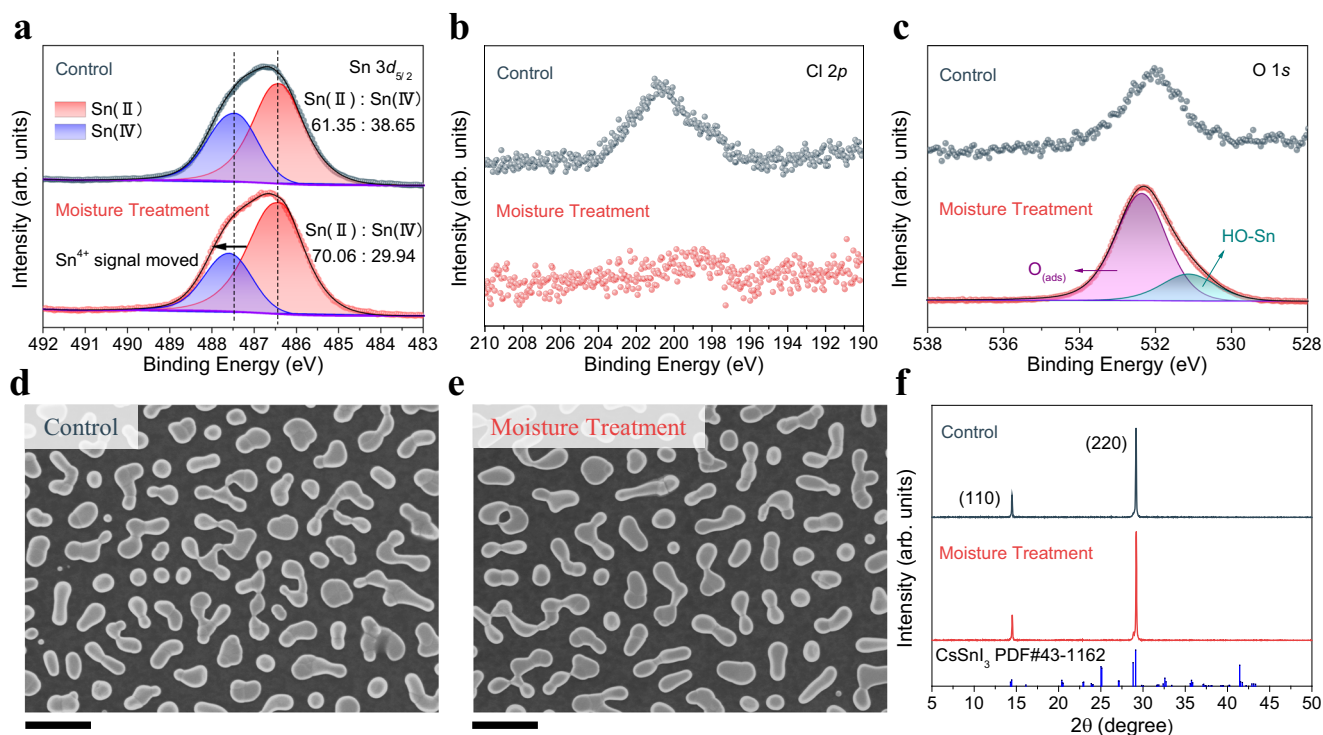


**Fig. 2 | The effect of moisture treatment on the perovskite film.** **a**  $\text{Sn } 3d_{5/2}$ , **(b)**  $\text{Cl } 2p$ , and **(c)**  $\text{O } 1s$  core-level XPS spectra of  $\text{CsSnI}_3\text{-SnCl}_2$  film before and after moisture treatment. Top-view SEM images of  $\text{CsSnI}_3\text{-SnCl}_2$  film **(d)** before and **(e)** after moisture treatment. Scale bar, 2  $\mu\text{m}$ . **f** XRD patterns of  $\text{CsSnI}_3\text{-SnCl}_2$  film before and after moisture treatment.

findings strongly confirm that  $\text{Sn(OH)}_4$  is indeed a product of  $\text{SnX}_4$  hydrolysis during moisture treatment.

Subsequently, to investigate the effects of moisture treatment on the morphology and structure of the  $\text{CsSnI}_3\text{-SnCl}_2$  films, we conducted

scanning electron microscopy (SEM), atomic force microscopy (AFM), and X-ray diffraction (XRD) measurements. SEM images revealed an island structure in the pristine  $\text{CsSnI}_3\text{-SnCl}_2$  film, and the structure hardly changed after moisture treatment (Fig. 2d-e). AFM images

further confirmed the persistence of the island structure following moisture treatment (Supplementary Fig. 8). The unchanged morphology is direct evidence that moisture treatment does not degrade the  $\text{CsSnI}_3\text{-SnCl}_2$  film, namely, the moisture hardly affects  $\text{Sn}^{2+}$ . XRD measurements further support this, demonstrating that moisture treatment does not alter the  $\text{CsSnI}_3$  lattice structure. In the XRD pattern, the  $\text{CsSnI}_3\text{-SnCl}_2$  film exhibits two diffraction peaks corresponding to the (110) and (220) facets of  $\text{B-}\gamma\text{-CsSnI}_3$  (PDF#43–1162) (Fig. 2f). Moreover, the diffraction intensity of (110) and (220) facets significantly increased after moisture treatment, suggesting that treatment effectively reduces lattice collapse by hydrolyzing  $\text{Sn}^{4+}$  in the  $\text{CsSnI}_3$  lattice. Crystallographic disorder, a potential source of non-radiative recombination centers that degrade device performance, could be mitigated by the moisture-triggered hydrolysis strategy.<sup>1</sup> These results provide compelling evidence that moisture treatment selectively hydrolyzes  $\text{SnX}_4$  without degrading the  $\text{CsSnI}_3$  structure, facilitating the construction of high-quality perovskite films.

### Optoelectronic properties after moisture treatment

Kelvin probe force microscopy (KPFM) was employed to characterize the potential distribution of the  $\text{CsSnI}_3\text{-SnCl}_2$  film. As depicted in Fig. 3a, b, the untreated  $\text{CsSnI}_3\text{-SnCl}_2$  film exhibited a surface potential of  $-0.123$  V compared with the m-PEDOT:PSS substrate. In contrast, the moisture-treated film exhibited a smaller surface potential of  $-0.053$  V, indicating a decrease in the surface potential after moisture treatment. A lower surface potential typically indicates a minor surface work function of the film, reflecting easier electron escape from the sample film. The reduced surface potential of the  $\text{CsSnI}_3\text{-SnCl}_2$  film suggests that moisture treatment effectively diminishes electron capture by eliminating  $\text{Sn}^{4+}$  defects.<sup>39</sup> To further investigate the carrier recombination dynamics in  $\text{CsSnI}_3\text{-SnCl}_2$  films, we conducted steady-state photoluminescence (PL) and time-resolved photoluminescence (TRPL) decay measurements. As shown in Fig. 3c, the PL intensity of the films significantly increased following moisture treatment, indicating a marked reduction in defect-mediated non-radiative recombination.<sup>40</sup>

The reduced defect-mediated non-radiative recombination was further supported by TRPL spectroscopy, in which the carrier lifetime was effectively prolonged after moisture treatment (Supplementary Fig. 9). A longer carrier lifetime generally implies fewer trap states in the perovskite film.<sup>41,42</sup>

We conducted photostability measurements to compare the stability of the films with and without moisture treatment. The untreated film exhibited poor stability, as evidenced by the noticeable weakening of PL intensity with extended continuous UV excitation (Fig. 3d). In contrast, after 300 min of continuous UV excitation, the PL intensity of the moisture-treated film remained virtually unchanged (Fig. 3e). The enhanced photostability can be attributed to a reduction in ionic mitigation channels, resulting from the elimination of  $\text{Sn}^{4+}$ -induced defects. Importantly, the enhanced stability underscores the advantages of all-inorganic Sn-based perovskite components, suggesting promising prospects for achieving stable NIR-II Pero-LEDs.

Additionally, to evaluate the impact of moisture treatment on the defect density in the films, we fabricated electron-only devices with the structure of ITO/  $\text{SnO}_2$ / Perovskite/ B3PYMPM/ LiF/ Al. The corresponding dark current density-voltage ( $J$ - $V$ ) curves are presented in Fig. 3f. The results indicate a significant decrease in the trap-filled limiting voltage ( $V_{\text{TFL}}$ ) of the device after moisture treatment, dropping from  $0.72$  V to  $0.46$  V. The defect density  $n_t$  in the films can be further calculated using Eq. (2).

$$n_t = 2\varepsilon\varepsilon_0 V_{\text{TFL}}/eL^2 \quad (2)$$

Where the  $\varepsilon$ ,  $\varepsilon_0$ ,  $e$ , and  $L$  represent the relative dielectric constant, vacuum permittivity, elementary charge, and thickness of the perovskite film, respectively. Calculations based on Eq. (2) reveal that the defect density significantly decreased from  $3.2 \times 10^{17} \text{ cm}^{-3}$  to  $2.13 \times 10^{17} \text{ cm}^{-3}$  following moisture treatment. These results collectively demonstrate that moisture treatment effectively reduces defect density associated with  $\text{Sn}^{4+}$  defects in the films, and the reduction defects are responsible for the observed improvement in PL intensity and

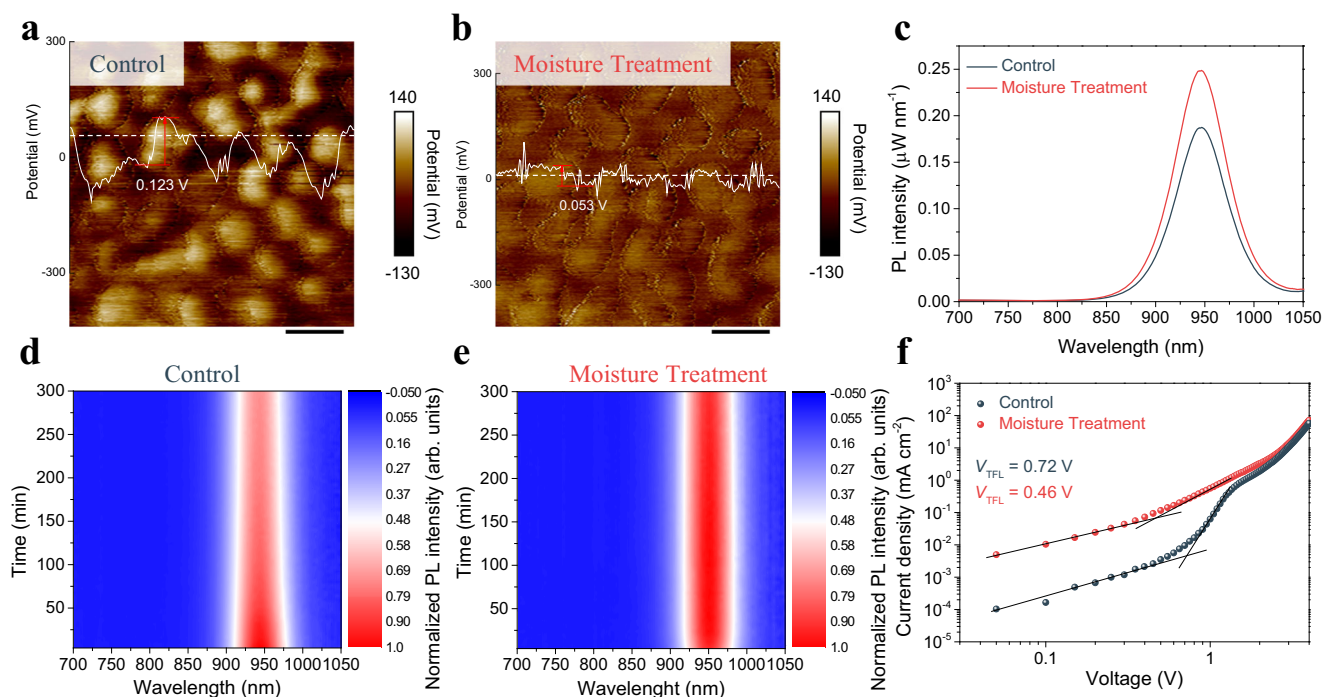


**Fig. 3 | The optoelectronic properties of  $\text{CsSnI}_3\text{-SnCl}_2$  film before and after moisture treatment. a, b** Kelvin probe force microscopy images. Scale bar,  $1 \mu\text{m}$ . **c** Photoluminescence spectra. **d, e** Photoluminescence spectra under continuous

UV excitation. **f** Dark  $J$ - $V$  curves of the electron-only devices with a structure of ITO/  $\text{SnO}_2$ / Perovskite/ SPPO13/ B3PYMPM/ LiF/ Al.



carrier lifetime. Besides, the current density of the electron-only device significantly increased after moisture treatment, indicating an enhancement in electron transport properties. This improvement is likely due to the reduction of  $\text{Sn}^{4+}$  defects within the lattice, a result of  $\text{SnX}_4$  hydrolysis. Previous reports suggest that the decrease of  $\text{Sn}^{4+}$  defects can effectively mitigate lattice collapse and decrease Sn vacancy, leading to improved crystal quality, which in turn enhances electron transport properties.<sup>27,28</sup> The conclusion is further supported by  $I$ - $V$  curves of the devices with a structure of ITO/ Perovskite/ Al (Supplementary Fig. 10). The conductivity of  $\text{CsSnI}_3$ - $\text{SnCl}_2$  film could be calculated by the equation of  $\sigma = Id/AV$ , where  $d$  is the thickness of the perovskite film and  $A$  is the device area. The results show an enhanced conductivity in the moisture-treated  $\text{CsSnI}_3$ - $\text{SnCl}_2$  film compared with the untreated one. These results suggest a strengthened electronic property in the moisture-treated  $\text{CsSnI}_3$ - $\text{SnCl}_2$  device.

### Enhancing the device performance by moisture treatment

Motivated by the remarkable improvement in film quality following moisture treatment, we proceeded to fabricate light-emitting diode devices. The Pero-LEDs are fabricated with a device structure of ITO/ m-PEDOT:PSS/ Perovskite/ SPPO13/ B3PYMPM/ LiF/ Al (Fig. 4a). The corresponding cross-sectional SEM image of the device is presented in Supplementary Fig. 11.

After moisture treatment, the radiance of Pero-LEDs is significantly enhanced, indicating that the non-radiative recombination associated with the  $\text{Sn}^{4+}$  defects is effectively reduced (Fig. 4b).<sup>43</sup> Simultaneously, the leakage current of Pero-LEDs noticeably decreased, indicating improved crystal quality and a reduction in defect-mediated pathways that typically contribute to leakage. This reduction in leakage current not only minimizes energy losses but also enhances the overall efficiency and stability of the device. Consequently, Pero-LEDs based on moisture treatment exhibited a substantial improvement in device performance, achieving an  $\text{EQE}_{\text{max}}$  of

7.61%, which is a 1.7-fold enhancement compared with that of pristine devices (4.5%) (Fig. 4c). We summarized the NIR-II Pero-LEDs and the corresponding results were presented in Supplementary Table 1. Additionally, the Pero-LEDs exhibited good electroluminescence (EL) stability, with the emissive peak at 945 nm remaining stable as the drive voltage increased (Fig. 4d). Furthermore, we presented the histogram of statistical EQEs by fabricating a series of Pero-LED devices. As shown in Fig. 4e, the moisture-treated Pero-LEDs exhibited good reproducibility, with an average EQE of 7.09%. Operational lifetime tests were conducted to evaluate the impact of moisture treatment on device stability (Fig. 4f). The operation lifetime of Pero-LEDs at a constant current density of  $20 \text{ mA cm}^{-2}$  achieved a remarkable half-lifetime of 82.6 h after moisture treatment, making a 3.7-fold increase compared with the untreated counterpart (22.3 h). The improved operation lifetime can be attributed to the reduction of ion migration channels due to the elimination of  $\text{Sn}^{4+}$  defects, thereby enhancing Pero-LEDs device performance. To account for the sensitivity of PEDOT:PSS to moisture treatment, we adopted an HTL-free device structure to isolate and verify the impact of moisture treatment on device performance. The experimental results exhibit that the radiance and EQE of Pero-LEDs also significantly improved as expected after moisture treatment (Supplementary Fig. 12). These findings collectively emphasize that moisture treatment can directly eliminate the  $\text{Sn}^{4+}$  defect in perovskite emitter, leading to enhanced film quality and device performance.

Additionally, we introduced  $\text{SnBr}_2$  and  $\text{SnI}_2$  as hydrolysis agents to replace  $\text{SnCl}_2$  and investigated the effect of different halide ions on eliminating  $\text{Sn}^{4+}$  defects within the  $\text{CsSnI}_3$  films via a moisture treatment strategy. According to the additional XRD (Supplementary Fig. 13) and PL (Supplementary Fig. 14) measurements of  $\text{CsSnI}_3$ - $\text{SnBr}_2$  and  $\text{CsSnI}_3$ - $\text{SnI}_2$  films, all these measurements consistently showed a similar and marked enhancement in crystallinity and PL intensity after moisture treatment. This highlights the universality of improving film

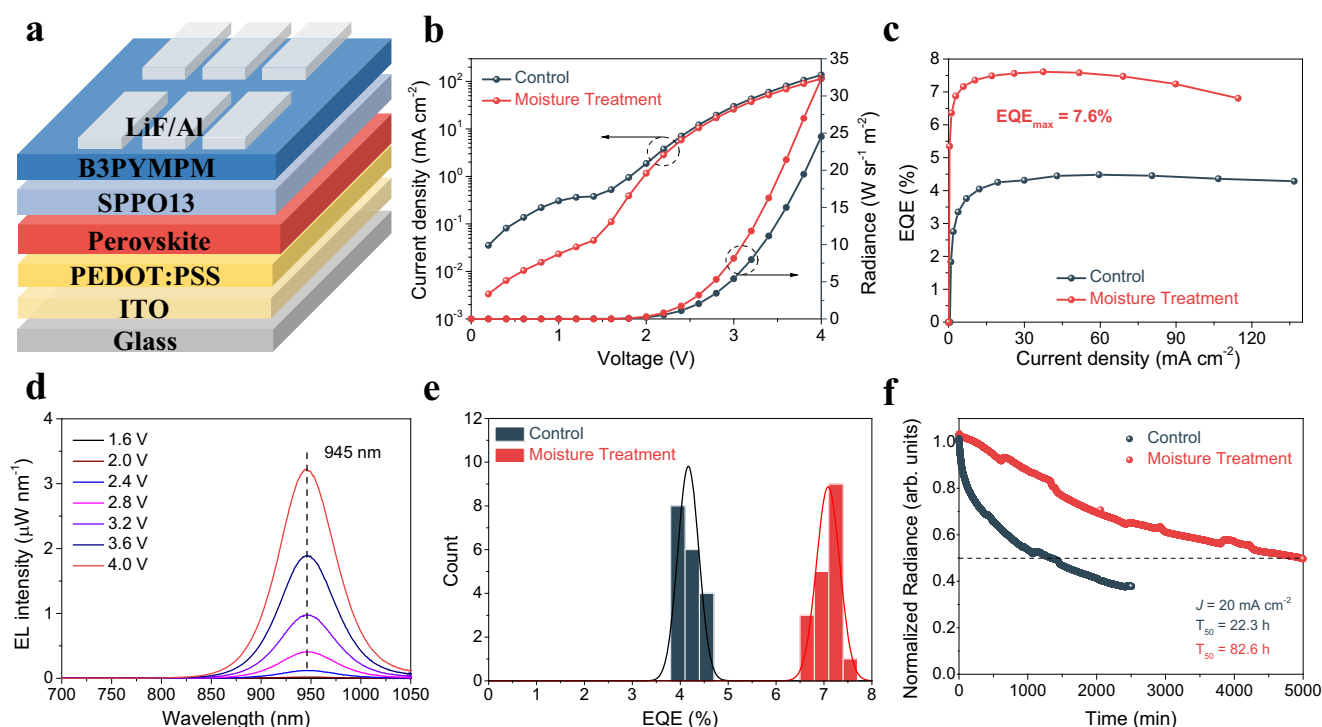


**Fig. 4 | The device performance of  $\text{CsSnI}_3$ - $\text{SnCl}_2$  Pero-LEDs with or without moisture treatment.** **a** Device structure illustration of the  $\text{CsSnI}_3$ -based Pero-LEDs. **b** Current density-voltage-radiance ( $J$ - $V$ - $R$ ) curves and **(c)** external quantum efficiency versus current density (EQE- $J$ ) curves of the Pero-LEDs.

**d** Electroluminescence spectra of the Pero-LEDs with moisture treatment at different operating voltages. **e** Statistical results of EQEs and **(f)** operation lifetime test results of the Pero-LEDs.

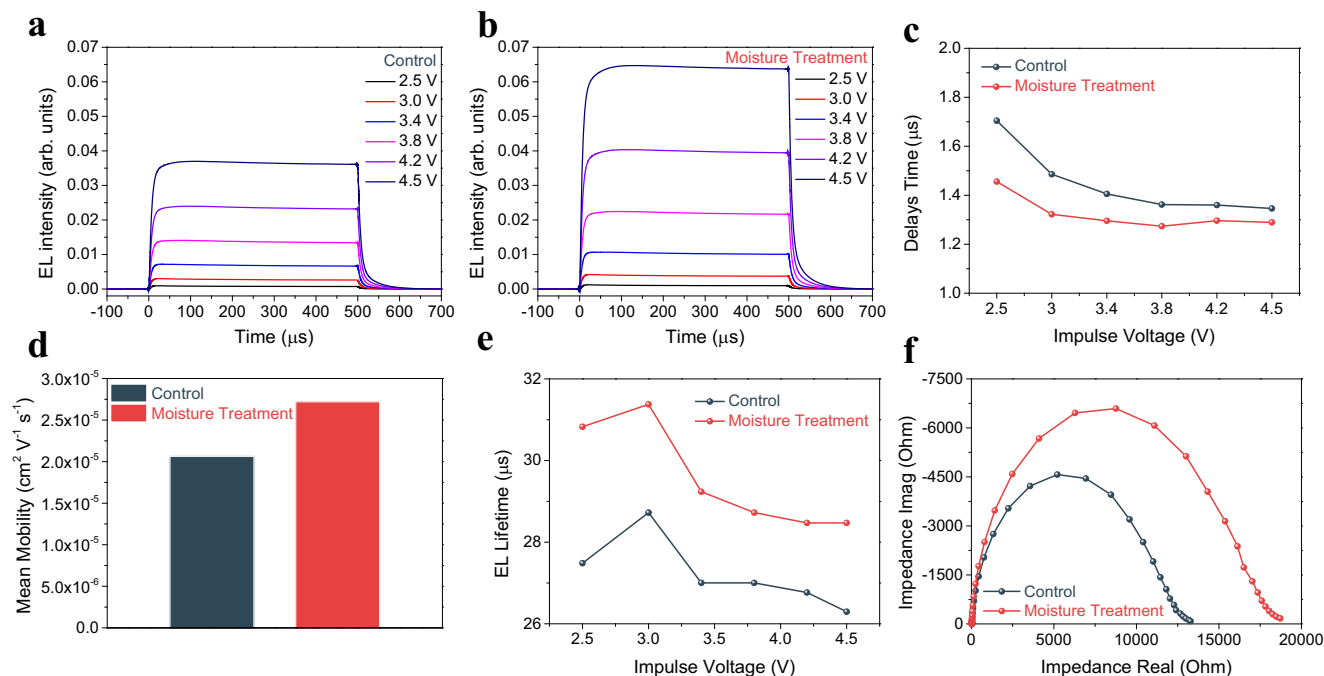


**Fig. 5 | The device physics of CsSnI<sub>3</sub>-SnCl<sub>2</sub> Pero-LEDs without or with moisture treatment. a, b** Applied various impulse voltage and resultant transient EL signals. **c** Delay time, obtained from the rising edge of the transient EL signal. **d** Estimated

electron mobility, obtained from the  $\Delta t_d$ . **e** Transient EL decay test, obtained from the falling edge of the transient EL signal. **f** Nyquist plots measured at turn-on voltage in dark conditions.

quality through moisture-triggered hydrolyzation of SnX<sub>4</sub>. Furthermore, Pero-LEDs based on CsSnI<sub>3</sub>-SnBr<sub>2</sub> and CsSnI<sub>3</sub>-SnI<sub>2</sub> were fabricated to investigate the impact of moisture treatment on device performance. Following moisture treatment, the CsSnI<sub>3</sub>-SnBr<sub>2</sub> and the CsSnI<sub>3</sub>-SnI<sub>2</sub> devices achieved an EQE<sub>max</sub> of 4.33% and 3.20%, respectively, which are 1.4-fold and 1.3-fold enhancement compared with that of the pristine device (Supplementary Fig. 15 and Supplementary Fig. 16). The marked enhancement in device efficiency further underscores the universality of the moisture treatment strategy in enhancing device performance. Based on the above results, it is concluded that moisture treatment is a universal strategy that could effectively eliminate Sn<sup>4+</sup>-induced defects in Sn-based perovskite film by moisture-triggered hydrolyzation of SnX<sub>4</sub>. Particularly, as the potent hydrolyzation agent for Sn<sup>4+</sup>, the Cl<sup>-</sup> could achieve the best Sn<sup>4+</sup> elimination effect due to its strong hydrolysis, thereby achieving more substantial improvement in the film quality and device performance based on Sn-based perovskite.

### Device physics of the Pero-LEDs

To delve deeper into the enhancement observed in device performance, we carried out the measurements in terms of device physics. Transient EL measurements were performed by applying various impulse voltages (Supplementary Fig. 17) and recording the resulting EL signals (Fig. 5a, b). The results indicate a notably stronger EL intensity in the moisture-treated device compared with the untreated counterpart, consistent with steady-state EL measurements, suggesting enhanced radiative recombination in the moisture-treated device. Moreover, delays time ( $\Delta t_d$ ), reflecting the time required for charge carrier to encounter and undergo radiative recombination following injection and transportation, were extracted from the rising edge of the transient EL signal (Fig. 5c).<sup>44</sup> These measurements revealed a smaller  $\Delta t_d$  value in the moisture-treated device compared with the control device, indicative of faster carrier injection into the emitting layer of LED devices, particularly for minority carriers. Previous studies have shown that large hole mobility and excess hole concentration in CsSnI<sub>3</sub>-based optoelectronic devices can cause electrons to behave as

minority carriers.<sup>16,45</sup> Thus, the electron mobility in the CsSnI<sub>3</sub> emitting layer was estimated using the following Eqs. (3) and (4).<sup>46</sup>

$$\mu_e = v/F = vd/V \quad (3)$$

$$v = d/t \quad (4)$$

Where  $v$  is the velocity of electrons,  $d$  is the thickness of the emitting layer,  $F$  is the electric field, and  $V$  is the driving voltage. The results indicated larger electron mobility in the moisture-treated sample ( $\sim 2.72 \times 10^{-5} \text{ cm}^2 \text{ V}^{-1} \text{ s}^{-1}$ ) compared with the pristine sample ( $\sim 2.06 \times 10^{-5} \text{ cm}^2 \text{ V}^{-1} \text{ s}^{-1}$ ), providing convincing evidence of improved electronic properties due to moisture treatment (Fig. 5d). The transient EL decay test showed an extended EL lifetime in moisture-treated device compared with the pristine device, indicating that emitting layer with fewer defects is conducive to photon exportation (Fig. 5e). The Nyquist plots exhibited an increase of the size of the arcs due to an enhanced recombination resistance in moisture-treated devices, indicative of reduced non-radiative recombination defects in the device (Fig. 5f).<sup>47,48</sup> This reduction also explains the improved PL intensity and EL intensity. Additionally, the series resistance of the device notably declined from  $37.4 \Omega$  to  $25.8 \Omega$  after moisture treatment, indicating a reduced charge injection barrier. This improvement can be attributed to the enhanced electronic properties, such as improved charge carrier mobility and reduced defects, facilitated by moisture treatment. These findings collectively demonstrate that moisture treatment effectively reduces non-radiative recombination defects and enhances electronic properties in CsSnI<sub>3</sub>-SnCl<sub>2</sub> Pero-LEDs devices.

In summary, we develop a targeted elimination strategy utilizing moisture-triggered hydrolysis of tin tetrahalide to remove Sn<sup>4+</sup> defects and improve the corresponding Pero-LEDs performance and stability. During the moisture treatment process, the detrimental Sn<sup>4+</sup> within the CsSnI<sub>3</sub> lattice is selectively hydrolyzed, yielding hydrolysis product Sn(OH)<sub>4</sub>, effectively eliminating the defects related to Sn<sup>4+</sup> without causing film degradation. Moreover, the formed Sn(OH)<sub>4</sub> can block the

oxidant erosion, providing sustaining protection for  $\text{Sn}^{2+}$  in the  $\text{CsSnI}_3$  film. Consequently, the crystal quality of  $\text{CsSnI}_3$  film is significantly enhanced, and the non-radiative recombination process is effectively suppressed, leading to substantial improvements in PL intensity and carrier lifetime. Subsequently, we fabricate Pero-LEDs with a NIR-II emission at 945 nm and significantly improved efficiency and stability. Pero-LEDs achieve a performance breakthrough with an  $\text{EQE}_{\text{max}}$  of 7.61% and a half-lifetime approaching 82.6 h. Notably, while moisture treatment achieves significant improvements in film quality and device performance, we recognize that not all  $\text{Sn}^{4+}$  defects, particularly those buried underneath or within a grain, have been completely removed. This is due to moisture primarily reacting with the  $\text{Sn}^{4+}$  in the  $\text{Sn}^{4+}$ -enriched film surface. Therefore, eliminating any remaining trace amounts of  $\text{Sn}^{4+}$  remains a priority for our future research to further enhance device performance. This study provides crucial insights into eliminating  $\text{Sn}^{4+}$  defects in films, paving the way for the development of efficient and stable Sn-based optoelectronic devices.

## Methods

### Materials

The materials used in this study all received without any purification. CsI (99.9%),  $\text{SnI}_2$  (99.999%),  $\text{SnCl}_2$  ( $\geq 99.9\%$ ), tin powder (particle size  $< 45 \mu\text{m}$ , 99.8%), DMSO (anhydrous,  $\geq 99.9\%$ ), chlorobenzene (99.9%), LiF (99.995%), and Poly(sodium 4-styrenesulfonate) powder (PSS:Na), all sourced from Sigma-Aldrich. Additionally, 4,6-Bis(3,5-di-3-pyridinylphenyl)-2-methylpyrimidine (B3PYMPM) was obtained from Luminescence Technology Corp, while Poly(3,4-ethylenedioxythiophene):poly(styrenesulfonate) (PEDOT:PSS, Clevios PVP AI4083) was acquired from Heraeus. 2,7-bis (diphenyl phosphoryl) - 9,9'-spirobifluorene (SPPO13) was sourced from Xi'an Polymer Technology Crop.

### Preparation of perovskite precursor solution

A precursor solution of  $\text{CsSnI}_3\text{-SnX}_2$  was prepared at a concentration of 0.25 M by dissolving a mixture of CsI,  $\text{SnI}_2$ , and  $\text{SnX}_2$  in DMSO, following a molar ratio of 1:1:0.1. To minimize the presence of  $\text{Sn}^{4+}$  ions, an additional 10 mg of tin powder was incorporated into the precursor solution. The resulting mixture was stirred at room temperature for at least 6 h. Ultimately, the solution was filtered through a  $0.1 \mu\text{m}$  PTFE filter, yielding a clear, transparent solution.

### Preparation of perovskite film

Perovskite films were fabricated through a spin-coating method, where the precursor solution was dripped onto substrates rotating at 4000 r.p.m. for 60 s. At the 30-s mark, 0.5 mL of chlorobenzene, which served as an antisolvent, was swiftly dripped onto the substrates. Following this, the coated substrates were transferred to a hotplate, where they were annealed at a temperature of  $110^\circ\text{C}$  for 10 min.

### Moisture treatment process

After the annealed perovskite films were cooled to room temperature, they were transferred to an airtight  $\text{N}_2$ -filled chamber. A bottle with saturated  $\text{K}_2\text{CO}_3$  aqueous solution in the  $\text{N}_2$ -filled chamber served as an  $\text{H}_2\text{O}$  source, providing a stable and low humidity of approximately 43 RH%. The films were treated with moisture for 10 min at room temperature and atmospheric pressure. The processed film and device were not annealed after the moisture treatment because the moisture provided only an infinitesimal amount of  $\text{H}_2\text{O}$  to the perovskite, avoiding the need for reannealing.

### Perovskite light-emitting diode device fabrication

The ITO substrates were subjected to an ultrasonic cleaning process, using a sequence of detergent solution, deionized water, isopropyl alcohol, and ethanol for 20 min each. They were treated in a plasma cleaner (Harrick, PDC-002-HP) for 7 min. To formulate the m-

PEDOT:PSS aqueous solution, PEDOT:PSS was mixed with a  $50 \text{ mg mL}^{-1}$  PSS:Na solution in a ratio of 1:1.2, stirred for 10 min, and filtered through a  $0.45 \mu\text{m}$  PTFE filter. The filtered m-PEDOT:PSS solution was spin-coated onto the cleaned substrates at 4000 r.p.m. for 40 s, followed by annealing at  $150^\circ\text{C}$  for 15 min. After annealing, the substrates were moved to a nitrogen-filled glove box for further processing. Perovskite films were deposited onto the m-PEDOT:PSS substrates as previously outlined. Following this, a  $4 \text{ mg mL}^{-1}$  SPPO13 solution in chlorobenzene was spin-coated onto the perovskite layer at 4000 r.p.m. for 60 s without annealing. The resulting films were then placed in a thermal evaporator, where B3PYMPM (50 nm), LiF (2 nm), and Al (80 nm) were deposited sequentially under a high vacuum of at least  $5 \times 10^{-4} \text{ Pa}$ . The active area of the device measures  $3 \text{ mm}^2$  ( $2 \text{ mm} \times 1.5 \text{ mm}$ ).

### Film and device characterization measurements

XRD patterns were recorded using the Smart Lab X-ray diffractometer (Rigaku Corporation) equipped with a  $\text{Cu K}\alpha$  radiation source. FTIR spectra were obtained from the Nicolet iS50 FTIR spectrometer (Thermo Scientific). AFM and KPFM results were acquired using the Bruker Multimode 8. A sample protection chamber was utilized during SEM and XPS measurements to prevent air exposure. SEM and XPS results were obtained from the JEOL JSM-7610F and the ThermoFisher ESCALAB Xi+, respectively. TRPL measurements were performed using fluorescence spectrometers (FLS-980), recording decay curves at 930 nm under 400 nm laser excitation. PL spectra were recorded using a QE-Pro spectrometer in a nitrogen-filled glove box. Transient EL measurements and electrical impedance spectroscopy measurements were conducted with a commercial system (Paios, FLUXiM). All device measurements were carried out in a nitrogen-filled environment, with careful calibration ensured, employing a Keithley 2400 instrument and a commercial system (XPQY-EQE, Guangzhou Xipu Optoelectronic Technology Co., Ltd.).

### Data availability

The raw data generated in this study are provided in the Source Data file. Source Data are provided with this paper. All data that support the findings of this study are available from the corresponding author upon request. Source data are provided with this paper.

## References

1. Sun, Y. et al. Bright and stable perovskite light-emitting diodes in the near-infrared range. *Nature* **615**, 830–835 (2023).
2. Wang, H. et al. Perovskite-molecule composite thin films for efficient and stable light-emitting diodes. *Nat. Commun.* **11**, 891 (2020).
3. Cao, Y. et al. Perovskite light-emitting diodes based on spontaneously formed submicrometre-scale structures. *Nature* **562**, 249–253 (2018).
4. Xu, W. et al. Rational molecular passivation for high-performance perovskite light-emitting diodes. *Nat. Photon.* **13**, 418–424 (2019).
5. Sun, L. et al. Bright infrared quantum-dot light-emitting diodes through inter-dot spacing control. *Nat. Nanotechnol.* **7**, 369–373 (2012).
6. Medintz, I. L., Uyeda, H. T., Goldman, E. R. & Mattoussi, H. Quantum dot bioconjugates for imaging, labelling and sensing. *Nat. Mater.* **4**, 435–446 (2005).
7. Borek, C. et al. Highly efficient, near-infrared electrophosphorescence from a Pt-metalloporphyrin complex. *Angew. Chem. Int. Ed. Engl.* **46**, 1109–1112 (2007).
8. Konstantatos, G. et al. Ultrasensitive solution-cast quantum dot photodetectors. *Nature* **442**, 180–183 (2006).
9. Welscher, K. et al. A route to brightly fluorescent carbon nanotubes for near-infrared imaging in mice. *Nat. Nanotechnol.* **4**, 773–780 (2009).
10. Sun, N. et al. Architecture of p-i-n Sn-based perovskite solar cells: characteristics, advances, and perspectives. *ACS Energy Lett.* **6**, 2863–2875 (2021).

11. Nasti, G. & Abate, A. Tin halide perovskite ( $\text{ASnX}_3$ ) solar cells: a comprehensive guide toward the highest power conversion efficiency. *Adv. Energy Mater.* **10**, 1902467 (2020).
12. Chung, I. et al.  $\text{CsSnI}_3$ : semiconductor or metal? High electrical conductivity and strong near-infrared photoluminescence from a single material. High hole mobility and phase-transitions. *J. Am. Chem. Soc.* **134**, 8579–8587 (2012).
13. Min, H. et al. Spin coating epitaxial heterodimensional tin perovskites for light-emitting diodes. *Nat. Nanotechnol.* **19**, 632–637 (2024).
14. Min, H. et al. Additive treatment yields high-performance lead-free perovskite light-emitting diodes. *Nat. Photon.* **17**, 755–760 (2023).
15. Akbulatov, A. F. et al. Comparative intrinsic thermal and photochemical stability of  $\text{Sn(II)}$  complex halides as next-generation materials for lead-free perovskite solar cells. *J. Phys. Chem. C* **123**, 26862–26869 (2019).
16. Lu, J. et al. Dendritic  $\text{CsSnI}_3$  for efficient and flexible near-infrared perovskite light-emitting diodes. *Adv. Mater.* **33**, e2104414 (2021).
17. Yuan, F. et al. Bright and stable near-infrared lead-free perovskite light-emitting diodes. *Nat. Photon.* **18**, 170–176 (2024).
18. Meng, Y. et al. Bi-functional phosphine oxide passivator for efficient near-infrared  $\text{sn}$ -based perovskite light-emitting diodes with ultra-low efficiency roll-off. *Adv. Funct. Mater.* **34**, 2310530 (2024).
19. Wu, T. et al. Lead-free tin perovskite solar cells. *Joule* **5**, 863–886 (2021).
20. Zhang, Z. et al. Mechanistic understanding of oxidation of tin-based perovskite solar cells and mitigation strategies. *Angew. Chem. Int. Ed. Engl.* **62**, e202308093 (2023).
21. Saidaminov, M. I. et al. Conventional solvent oxidizes  $\text{Sn(II)}$  in perovskite inks. *ACS Energy Lett.* **5**, 1153–1155 (2020).
22. Guan, X. et al. Suppressing disproportionation decomposition in  $\text{Sn}$ -based perovskite light-emitting diodes. *ACS Energy Lett.* **8**, 1597–1605 (2023).
23. Liu, J. et al. Origins and suppression of  $\text{Sn(II)/Sn(IV)}$  oxidation in tin halide perovskite solar cells. *Adv. Energy Mater.* **13**, 2300696 (2023).
24. Di Girolamo, D. et al. Solvents for processing stable tin halide perovskites. *ACS Energy Lett.* **6**, 959–968 (2021).
25. Li, G. X. et al. Ionic liquid stabilizing high-efficiency tin halide perovskite solar cells. *Adv. Energy Mater.* **11**, 2101539 (2021).
26. Li, Y. et al. Boosting  $\text{CsSnI}_3$ -based near-infrared perovskite light-emitting diodes performance via solvent coordination engineering. *InfoMat* **6**, e12537 (2024).
27. Ye, T. et al. Ambient-air-stable lead-free  $\text{CsSnI}_3$  solar cells with greater than 7.5% efficiency. *J. Am. Chem. Soc.* **143**, 4319–4328 (2021).
28. Ye, T. et al. Localized electron density engineering for stabilized B-Y  $\text{CsSnI}_3$ -based perovskite solar cells with efficiencies >10%. *ACS Energy Lett.* **6**, 1480–1489 (2021).
29. Tai, Q. et al. Antioxidant grain passivation for air-stable tin-based perovskite solar cells. *Angew. Chem. Int. Ed.* **58**, 806–810 (2019).
30. Nakamura, T. et al.  $\text{Sn(IV)}$ -free tin perovskite films realized by in situ  $\text{Sn(O)}$  nanoparticle treatment of the precursor solution. *Nat. Commun.* **11**, 3008 (2020).
31. Zhou, J. et al. Chemo-thermal surface dedoping for high-performance tin perovskite solar cells. *Matter* **5**, 683–693 (2022).
32. Nishimura, K. et al. Lead-free tin-halide perovskite solar cells with 13% efficiency. *Nano Energy* **74**, 104858 (2020).
33. Heo, Y. J. et al. Enhancing performance and stability of tin halide perovskite light emitting diodes via coordination engineering of lewis acid-base adducts. *Adv. Funct. Mater.* **31**, 2106974 (2021).
34. Lanzetta, L. et al. Degradation mechanism of hybrid tin-based perovskite solar cells and the critical role of tin (IV) iodide. *Nat. Commun.* **12**, 2853 (2021).
35. Zhou, H. et al. 24.96%-efficiency  $\text{FACsPbI}_3$  perovskite solar cells enabled by an asymmetric 1,3-thiazole-2,4-diammonium. *Adv. Energy Mater.* **13**, 2204372 (2023).
36. Li, Y. et al. Transport layer engineering by hydrochloric acid for efficient perovskite solar cells with a high open-circuit voltage. *ACS Appl. Mater. Interfaces* **15**, 23208–23216 (2023).
37. El Hachmi, A. et al. Structural, morphological, magnetic and optical properties of Jeanbandyite prepared by the co-precipitation method. *Mater. Today Commun.* **34**, 105358 (2023).
38. Yang, D. et al. Synthesis and properties of  $\text{SrSn(OH)}_6$  nanorods and their flame retardancy and smoke suppression effects on epoxy resin. *J. Coat. Technol. Res* **16**, 1715–1725 (2019).
39. Hu, M. et al. Surface  $\text{Sn(IV)}$  hydrolysis improves inorganic  $\text{Sn-Pb}$  perovskite solar cells. *ACS Energy Lett.* **8**, 1035–1041 (2023).
40. Ma, D. et al. Distribution control enables efficient reduced-dimensional perovskite LEDs. *Nature* **599**, 594–598 (2021).
41. Lin, K. B. et al. Dual-phase regulation for high-efficiency perovskite light-emitting diodes. *Adv. Funct. Mater.* **32**, 2200350 (2022).
42. Lin, K. et al. Perovskite light-emitting diodes with external quantum efficiency exceeding 20 percent. *Nature* **562**, 245–248 (2018).
43. Li, M. et al. Conductive phosphine oxide passivator enables efficient perovskite light-emitting diodes. *Nano Lett.* **22**, 2490–2496 (2022).
44. Jenatsch, S., Züfle, S., Blülle, B. & Ruhstaller, B. Combining steady-state with frequency and time domain data to quantitatively analyze charge transport in organic light-emitting diodes. *J. Appl. Phys.* **127**, 031102 (2020).
45. Liu, A. et al. High-performance inorganic metal halide perovskite transistors. *Nat. Electron* **5**, 78–83 (2022).
46. Kim, J., Hahm, D., Bae, W. K., Lee, H. & Kwak, J. Transient dynamics of charges and excitons in quantum dot light-emitting diodes. *Small* **18**, e2202290 (2022).
47. Yudco, S., Bisquert, J. & Etgar, L. Enhanced LED performance by ion migration in multiple quantum well perovskite. *J. Phys. Chem. Lett.* **14**, 11610–11617 (2023).
48. Liu, Z. et al. Perovskite light-emitting diodes with EQE exceeding 28% through a synergetic dual-additive strategy for defect passivation and nanostructure regulation. *Adv. Mater.* **33**, 2103268 (2021).

## Acknowledgements

X.G. and Y.Q.L. contributed equally to this work. This work is financially supported by the National Key Research and Development Program of China (2022YFA1204800), National Natural Science Foundation of China (U21A2078, 22179042, and 12104170), Scientific Research Funds of Huaqiao University, and subsidized Project for Postgraduate's Innovative Fund in Scientific Research of Huaqiao University.

## Author contributions

X. Guan and Y. Q. Li carried out the device fabrication and characterizations of Pero-LEDs. X. Guan, Y. Q. Li, and Y. Y. Meng contributed to the device optimization and conducted a device stability test. X. Guan contributed to the XPS measurements and result analysis. K. X. Wang, Y. J. Luo, and K. B. Lin contributed to the optical measurements and result analysis, including PL and TRPL decay tests. J. Wang contributed to the XRD measurements. Z. T. Duan and H. Liu carried out the SEM and cross-sectional SEM. L. Yang contributed to the KPFM measurements. L. F. Zheng fabricated electron-only devices and analyzed the dark  $J$ - $V$  curves. J. P. Lin and Y. L. Weng drew the schematics. X. Guan and J. X. Lu wrote the manuscript. All authors discussed the results and commented on the manuscript. F. X. Xie, J. X. Lu, and Z. H. Wei supervised the project.

## Competing interests

The authors declare no competing interests.



## Additional information

**Supplementary information** The online version contains supplementary material available at <https://doi.org/10.1038/s41467-024-54160-x>.

**Correspondence** and requests for materials should be addressed to Fengxian Xie, Jianxun Lu or Zhanhua Wei.

**Peer review information** *Nature Communications* thanks Zhi-Kuang Tan and the other anonymous reviewer(s) for their contribution to the peer review of this work. A peer review file is available.

**Reprints and permissions information** is available at <http://www.nature.com/reprints>

**Publisher's note** Springer Nature remains neutral with regard to jurisdictional claims in published maps and institutional affiliations.

**Open Access** This article is licensed under a Creative Commons Attribution-NonCommercial-NoDerivatives 4.0 International License, which permits any non-commercial use, sharing, distribution and reproduction in any medium or format, as long as you give appropriate credit to the original author(s) and the source, provide a link to the Creative Commons licence, and indicate if you modified the licensed material. You do not have permission under this licence to share adapted material derived from this article or parts of it. The images or other third party material in this article are included in the article's Creative Commons licence, unless indicated otherwise in a credit line to the material. If material is not included in the article's Creative Commons licence and your intended use is not permitted by statutory regulation or exceeds the permitted use, you will need to obtain permission directly from the copyright holder. To view a copy of this licence, visit <http://creativecommons.org/licenses/by-nc-nd/4.0/>.

© The Author(s) 2024